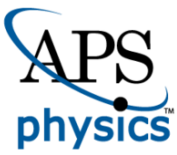

Scale invariance of parity-invariant three-dimensional QED

Nikhil Karthik and Rajamani Narayanan

Phys. Rev. D **94**, 065026 — Published 21 September 2016

DOI: 10.1103/PhysRevD.94.065026

Scale-invariance of parity-invariant three-dimensional QED

Nikhil Karthik* and Rajamani Narayanan†

Department of Physics, Florida International University, Miami, FL 33199.

(Dated: August 23, 2016)

Abstract

We present numerical evidences using overlap fermions for a scale-invariant behavior of parity-invariant three-dimensional QED with two flavors of massless two-component fermions. Using finite-size scaling of the low-lying eigenvalues of the massless anti-Hermitian overlap Dirac operator, we rule out the presence of bilinear condensate and estimate the mass anomalous dimension. The eigenvectors associated with these low-lying eigenvalues suggest critical behavior in the sense of a metal-insulator transition. We show that there is no mass gap in the scalar and vector correlators in the infinite volume theory. The vector correlator does not acquire an anomalous dimension. The anomalous dimension associated with the long-distance behavior of the scalar correlator is consistent with the mass anomalous dimension.

PACS numbers: 11.15.Ha, 11.10.Kk, 11.30.Qc

*Electronic address: nkarthik@fiu.edu

†Electronic address: rajamani.narayanan@fiu.edu

I. INTRODUCTION

Two-component massless fermions coupled to a three-dimensional Euclidean abelian gauge field has been a topic of study in the past three decades for several field-theoretic reasons. The presence of parity anomaly [1–4] induces a topological mass term for the gauge fields. Soon after that, it found an application in condensed matter physics as a possible explanation of the quantum Hall effect [5]. Recently, duality between various theories in three dimensions that includes fermions coupled to abelian gauge fields with or without Chern-Simons matter are being discussed in the context of condensed matter physics [6, 7]. Of particular interest to us in this paper is the possible conformal nature of parity-invariant theories with even number, $2N_f$, of massless flavors. This could have implications in the conductivity of graphene type materials [8, 9]. Also, the $N_f = 2$ theory seems to be of interest in the context of high-T_c cuprates [10, 11].

A simple analysis of the associated gap equation [12] suggested that fermions could generate a mass as the number of flavors tends to infinity. Subsequent analysis of the gap equation [13–16] reached an opposite conclusion that the infra-red behavior of the large-N_f theory is scale-invariant due to the presence of a non-trivial fixed point. However, it also lead to the possibility of a non-zero bilinear condensate if $N_f < 4$, and the conclusion remained stable when $1/N_f$ correction was included [17]. A computation of renormalization group flow including the presence of parity-invariant four-fermion terms, lead to a critical number of flavors in the region of $N_f = 4$ to $N_f = 10$ [18]. Comparing the free energies in the IR and UV assuming non-interacting particles, one finds that symmetry breaking is not expected when $N_f > 3/2$ [19, 20]. Recently, there has been a renewed interest in parity-invariant QED_3 due to the presence of Wilson-Fisher fixed point in $4 - \epsilon$ dimensions. A similar comparison of the free energies, now assuming a conformal phase and a broken phase, suggests that symmetry is not broken when $N_f > 4$ [21]. A computation [22] of the coefficient of the two-point function of the stress energy tensor in the $4 - \epsilon$ expansion supports a conformal phase if $N_f > 1 + \sqrt{2}$. Computations [23, 24] of the scaling dimensions of the naively irrelevant four-fermion operators in the vicinity of the Wilson-Fisher fixed point suggest that the four-fermion operators become relevant for $N_f < 2$, and hence the possibility that the infra-red fixed point becomes unstable for $N_f < 2$. A computation [25] of the scaling dimensions of the parity-even four-fermion operators in a $1/N_f$ expansion, taking into account the mixing with a larger basis of operators, suggests that theories with $N_f > 1$ are conformal.

Earlier numerical work that studied the behavior of the fermion bilinear as a function of the

fermion mass using staggered fermions [26, 27] indicated that there is evidence for a bilinear condensate for $N_f = 1$. The evidence for a condensate in $N_f = 2$ was found to be weak. A numerical study [28] of the beta function for $N_f = 2$ theory with Wilson fermions indicated that this is theory is not probably conformal [1]. A recent study [29] of the spectrum of the low-lying eigenvalues of the massless Wilson-Dirac operator did not show any evidence for condensate for $N_f \geq 1$.

The continuum fermion action is

$$S_f = \int d^3x \sum_{i=1}^{N_f} [\bar{\chi}_{+i} C \chi_{+i} + \bar{\chi}_{-i} C \chi_{-i}]\,; \quad C = \sum_{k=1}^{3} \sigma_k \{\partial_k + i A_k(x)\}\,; \quad C^\dagger = -C, \tag{1}$$

where $\chi_{\pm i}$ are the two-component fermion fields. Of particular relevance is the U($2N_f$) global symmetry formally present in the continuum fermion action:

$$\begin{pmatrix} \chi_+ \\ \chi_- \end{pmatrix} \to S \begin{pmatrix} \chi_+ \\ \chi_- \end{pmatrix} \quad \text{and} \quad \begin{pmatrix} \bar{\chi}_+ & \bar{\chi}_- \end{pmatrix} \to \begin{pmatrix} \bar{\chi}_+ & \bar{\chi}_- \end{pmatrix} S^\dagger, \quad \text{where} \quad S \in \mathrm{U}(2N_f). \tag{2}$$

Keeping in mind that the regularization will preserve parity, we rewrite the fermion action as

$$S_f = \int d^3x \sum_{i=1}^{N_f} \left[\bar{\chi}_{+i} C \chi_{+i} - \bar{\chi}_{-i} C^\dagger \chi_{-i}\right], \tag{3}$$

which is invariant under the parity transformation,

$$C \to C^\dagger; \quad \chi_{+i} \leftrightarrow \chi_{-i}; \quad \bar{\chi}_{+i} \leftrightarrow -\bar{\chi}_{-i}. \tag{4}$$

The U($2N_f$) symmetry is broken to U(N_f)×U(N_f) if one uses Wilson fermions as a regulator on the lattice, and it is only recovered in the continuum limit for massless fermions. Indeed, the numerical computations in [29] were done such that the continuum limit was taken at a fixed physical volume and the infinite volume limit was subsequently studied. As we will show in this paper, the U($2N_f$) symmetry is present at the lattice level if one uses overlap fermions. This is also the case if one regulates using domain wall fermions [30, 31] and take the limit of infinite number of fermions in the extra direction.

Since the overlap formalism in odd dimensions [32, 33] is not as well known as in even dimensions, we start with an introduction to overlap fermions in Section II. We point out the

[1] We think that one can use the data presented in Table-II of [28] and reach a conclusion that $N_f = 2$ theory has an IR fixed point. The value of physical size of the box, ℓ as defined in this paper, corresponding to the values of β and L in [28] is $\ell = 2L/\beta$. A linear behavior can be seen in a plot of the inverse of the dimensionless renormalized coupling, $1/g^2$, versus $1/\ell$ that includes their data from all L. A non-zero intercept at $1/\ell = 0$ seen in their data suggests the existence of the IR fixed point at $g_c^2 \approx 48$.

U($2N_f$) symmetry present at the level of the generating functional for massless overlap fermions in a gauge field background. We perform numerical simulations using massless overlap fermions for the case of $N_f = 1$ and extract continuum results in a periodic box of size, ℓ^3. Our aim is to show that the $N_f = 1$ theory is scale-invariant. We explore three aspects of the theory to establish scale invariance:

1. If the low-lying eigenvalues λ of the massless anti-Hermitian overlap operator depend on the finite physical size ℓ as

$$\lambda \sim \ell^{-1-\gamma_m} \tag{5}$$

with $\gamma_m < 2$, then there is no bilinear condensate in the infinite volume theory and the exponent γ_m is the mass anomalous dimension. We will show that $\gamma_m = 1.0 \pm 0.2$ in Section IV. This is at the edge of the maximum allowed value for γ_m in a theory which is also conformally invariant [34].

2. In the sense of a metal-insulator transition [35–38], we will show that the eigenvectors associated with the low lying eigenvalues lie in the critical regime. The inverse participation ratio (IPR) of the eigenvectors Ψ_λ is defined as

$$I_2 = \frac{\int \{\Psi^*_\lambda(x)\Psi_\lambda(x)\}^2 d^3x}{\int \Psi^*_\lambda(x)\Psi_\lambda(x) d^3x}. \tag{6}$$

In the critical regime, the IPR would exhibit a scaling with the physical size ℓ as

$$I_2 \sim \ell^{-3+\eta}. \tag{7}$$

This scaling is related to the behavior of the number variance $\Sigma_2(n)$, the variance of the number of eigenvalues, n, below a given value, λ. In the critical regime, $\Sigma_2(n)$ would exhibit an asymptotic linear behavior with a slope $\eta/6$:

$$\Sigma_2(n) = \frac{\eta}{6} n. \tag{8}$$

We will demonstrate in Section V that the low-lying eigensystem of the $N_f = 1$ theory satisfy such a critical behavior with $\eta = 0.38(1)$.

3. We study the correlators of parity-even vector bilinear,

$$V_k(x) = \bar{\chi}_+(x)\sigma_k\chi_+(x) - \bar{\chi}_-(x)\sigma_k\chi_-(x), \tag{9}$$

and the scalar bilinear

$$\Sigma(x) = \bar{\chi}_+(x)\chi_+(x) - \bar{\chi}_-(x)\chi_-(x), \tag{10}$$

in Section VI. In both the cases, we will show there is no mass gap in their spectrum, and that the long-distance behavior of the correlators at zero spatial momentum exhibits a power-law. The power-law associated with the vector correlator does not acquire any anomalous dimension consistent with the vector bilinear being a conserved current. The scalar correlator does not show a simple power-law behavior as a function of Euclidean time, leading us to estimate the expected power-law at even longer distances inaccessible to our numerical simulation. The resulting value for the mass anomalous dimension is $\gamma_m = 0.8(1)$ which is consistent with the result from the low lying eigenvalues and consistent with a vanishing correlator in the long distance limit.

II. OVERLAP FORMALISM IN THREE DIMENSIONS

The overlap formalism for two-component fermions in three dimensions were originally discussed in [32, 33] and more recently for parity-invariant four-component fermions by starting from domain wall fermions [30, 31]. In this paper, we start from the original overlap formalism [39] to obtain the result in three dimensions. In this manner, we will explicitly show the parity-invariant factorization into two two-component fermions.

A. Gauge-invariant but parity-breaking overlap operator for a single flavor of two-component massless fermion

The overlap formula [39] for a two-component fermion determinant in three dimensions is

$$\det C_o = \langle 0 - | 0 + \rangle, \tag{11}$$

where $|0\pm\rangle$ are the lowest states of the many body operators,

$$\mathcal{H}_\pm = -\begin{pmatrix} a^\dagger & b^\dagger \end{pmatrix} H_\pm \begin{pmatrix} a \\ b \end{pmatrix}, \tag{12}$$

with $(a^\dagger, b^\dagger)$ and (a, b) being two-component fermion creation and annihilation operators that obey canonical anti-commutation relations. The two single particle Hamiltonians are

$$H_+ = \begin{pmatrix} B & D \\ -D & -B \end{pmatrix}; \qquad H_- = \gamma_5 = \begin{pmatrix} 1 & 0 \\ 0 & -1 \end{pmatrix}. \tag{13}$$

The naïve massless Dirac operator in three dimensions is

$$D = \frac{1}{2}\sum_{k=1}^{3} \sigma_k \left(T_k - T_k^\dagger \right); \qquad \left(T_k \phi\right)(x) = U_k(x)\phi(x + \hat{k}); \qquad T_k^\dagger T_k = 1. \tag{14}$$

with σ_k; $k = 1, 2, 3$ being the two-component Pauli matrices. The standard Wilson term is

$$B = \frac{1}{2}\sum_{k=1}^{3}\left(2 - T_k - T_k^\dagger\right) - m_w; \qquad B = B^\dagger, \tag{15}$$

with a Wilson mass parameter in the range $0 < m_w < 2$.

The naïve massless Dirac operator in three dimensions is anti-Hermitian; $D^\dagger = -D$. Due to this special structure of H_+ in Eq. (13), one can obtain an expression for $\langle 0 - |0+\rangle$ in odd dimensions in terms of an explicit operator. Defining

$$X = B + D, \tag{16}$$

we can set up the following eigenvalue problems:

$$X^\dagger X\mathcal{R} = \mathcal{R}\Lambda^2; \qquad XX^\dagger\mathcal{L} = \mathcal{L}\Lambda^2; \qquad \Lambda_{ij} = \lambda_i\delta_{ij}; \qquad \lambda_i > 0. \tag{17}$$

It follows that

$$X = \mathcal{L}\Lambda\mathcal{R}^\dagger; \qquad V \equiv \mathcal{L}\mathcal{R}^\dagger = X\frac{1}{\sqrt{X^\dagger X}} = \frac{1}{\sqrt{XX^\dagger}}X; \qquad VV^\dagger = 1. \tag{18}$$

The basis of positive and negative eigenstates of H_+ are

$$\frac{1}{2}\begin{pmatrix}(1+V)\mathcal{R}\\(1-V)\mathcal{R}\end{pmatrix}; \qquad \frac{1}{2}\begin{pmatrix}(1-V)\mathcal{R}\\(1+V)\mathcal{R}\end{pmatrix}; \tag{19}$$

respectively. On the one hand, the basis of positive and negative eigenstates of H_- can be chosen to be

$$\begin{pmatrix}\mathcal{R}\\0\end{pmatrix}; \qquad \begin{pmatrix}0\\\mathcal{R}\end{pmatrix}; \tag{20}$$

respectively and the fermion determinant for a single two-component fermion becomes

$$\det C_o = \det\frac{1+V}{2}. \tag{21}$$

On the other hand, the basis of positive and negative eigenstates of H_- can be chosen to be

$$\begin{pmatrix}\mathcal{L}\\0\end{pmatrix}; \qquad \begin{pmatrix}0\\\mathcal{L}\end{pmatrix}; \tag{22}$$

respectively and the fermion determinant for a single two-component fermion becomes

$$\det C_o = \det\frac{1+V^\dagger}{2}. \tag{23}$$

In both cases, the fermion determinant is gauge invariant [33]. The phase of the fermion determinant arises from the phase of the Wilson-Dirac operator X analyzed in detail in [40] and carries the parity anomaly [32, 33].

B. U($2N_f$) symmetric parity and gauge-invariant overlap formalism

In order to realize a parity-invariant theory, we consider theories with even number of fermion flavors, $2N_f$. As shown in Appendix B, the result for the generating function for a $N_f = 1$ theory, including parity invariant fermion masses and using flavor diagonal sources η_+ and η_-, is

$$Z_2(\eta_+, \eta_-, \bar{\eta}_+, \bar{\eta}_-; m) = \{\det C_o(m) \exp\left[\bar{\eta}_+ G_o(m) \eta_+\right]\} \left\{\det C_o^\dagger(m) \exp\left[-\bar{\eta}_- G_o^\dagger(m) \eta_-\right]\right\}, \quad (24)$$

where

$$C_o(m) = \frac{1+V}{2} + m\frac{1-V}{2}; \qquad G_o(m) = \frac{1}{1-m}\left[C_o^{-1}(m) - 1\right] = \frac{A}{1+mA}, \quad (25)$$

and

$$A = \frac{1-V}{1+V}; \quad A = -A^\dagger. \quad (26)$$

The generating functional for the massless fermions is

$$Z_2(\eta_+, \eta_-, \bar{\eta}_+, \bar{\eta}_-; 0) = \det\left(C_o(0) C_o^\dagger(0)\right) \exp\left[\bar{\eta}_+ A \eta_+ + \bar{\eta}_- A \eta_-\right]. \quad (27)$$

Like in the continuum, the generating functional is invariant under the full U(2) symmetry,

$$\begin{pmatrix} \eta_+ \\ \eta_- \end{pmatrix} \to S \begin{pmatrix} \eta_+ \\ \eta_- \end{pmatrix} \quad \text{and} \quad \begin{pmatrix} \bar{\eta}_+ & \bar{\eta}_- \end{pmatrix} \to \begin{pmatrix} \bar{\eta}_+ & \bar{\eta}_- \end{pmatrix} S^\dagger, \quad \text{where} \quad S \in \mathrm{U}(2), \quad (28)$$

and also invariant under the parity transformation,

$$A \to A^\dagger; \quad \eta_+ \leftrightarrow \eta_-; \quad \bar{\eta}_+ \leftrightarrow -\bar{\eta}_-. \quad (29)$$

The fermion determinant in the absence of sources for the massless $N_f = 1$ theory is

$$\det \frac{1+V}{2} \det \frac{1+V^\dagger}{2} = \det V^\dagger \det \left[\frac{1+V}{2}\right]^2. \quad (30)$$

This also shows a U(2) symmetry, but we have an additional factor of $\det V^\dagger$ in the measure for the gauge fields, which is required to keep the theory parity invariant.

C. Eigenvalues of the overlap operator

The bilinear scalar condensate in a fixed gauge field background is given by

$$\Sigma(m) = \frac{1}{2\ell^3} \int \langle \Sigma(x) \rangle d^3x = \frac{1}{2\ell^3} \mathrm{tr}\ \left[G_o(m) + G_o^\dagger(m)\right] = \int_{-\infty}^{\infty} d\Lambda \frac{\rho(\Lambda)}{i\Lambda + m}, \quad \int_{-\infty}^{\infty} \rho(\Lambda) = 1; \quad (31)$$

where $i\Lambda$ are the eigenvalues of A^{-1} and $\rho(\Lambda)$ is the density of eigenvalues obeying $\rho(\Lambda) = \rho(-\Lambda)$. Therefore, we are led to an analysis of the low-lying eigenvalues of A^{-1} in order to extract the mass anomalous dimension.

Given an eigenvalue $e^{i\Phi_i}$ of V, the corresponding eigenvalue of A^{-1} is

$$i\Lambda_i = i \cot \frac{\Phi_i}{2}. \tag{32}$$

Therefore, the low-lying eigenvalues come from values of Φ_i close to π. In order to obtain these numerically using the Ritz algorithm [41], we compute the low-lying eigenvalues of the positive definite operator,

$$C_0(0)C_0^\dagger(0) = \frac{2 + V + V^\dagger}{4}. \tag{33}$$

The corresponding eigenvalue of this operator is $\cos^2 \frac{\Phi_i}{2}$. Due to parity invariance, we only need

$$|\Lambda_i| = \frac{|\cos \frac{\Phi_i}{2}|}{\sqrt{1 - \cos^2 \frac{\Phi_i}{2}}}. \tag{34}$$

III. SET UP OF THE NUMERICAL CALCULATION

The numerical details essentially parallel the one used in our previous work [29] with Wilson fermions. The only new ingredient is the presence of the operator V defined in Eq. (18). We used a 21$^{\text{st}}$ order Zolotarev approximation [42, 43] to realize $\frac{1}{\sqrt{X^\dagger X}}$ and this was sufficient for all our simulation parameters. We worked with massless fermions and the pseudofermion operator was written as

$$S_f(\phi) = \left(C_o^{-1}(0)\phi\right)^\dagger C_o^{-1}(0)\phi = \phi^\dagger \frac{4}{2 + V + V^\dagger}\phi. \tag{35}$$

We would like to draw attention to the advantage of using two-flavors of two component fermions instead of using an equivalent single four-component fermion formalism; the fermion determinant is a determinant of a positive-definite operator enabling the Monte Carlo simulation for any value of $2N_f$. We worked on a 3d torus of fixed physical extent ℓ and regulated using a L^3 lattice. The relation to the standard lattice gauge coupling is $\beta = 2L/\ell$ as seen in Eq. (C1) in Appendix C. Since it is a bit different from the standard procedure, we note that L is used to tune the lattice spacing at a fixed physical size, ℓ. We used $L = 12, 14, 16, 20$ and 24 to extract the continuum limit of observables. It is worth noting that unlike in four dimensions, there could be $\mathcal{O}(1/L)$ corrections due to the presence of parity-even, dimension-four, four-fermion operators which preserve the U($2N_f$) flavor symmetry. We used several different values of ℓ to understand the behavior of the theory as a function of ℓ, and then properly obtain the behavior as $\ell \to \infty$. We list our simulation points in the Appendix C.

In order to take the continuum limit, one has to take into account a factor arising from the Wilson mass parameter to realize the correct dispersion relation for free fermions [44]. At a finite lattice spacing, this factor can be improved and we define the improved eigenvalues by

$$\lambda_i = Z_m \Lambda_i \quad ; \quad Z_m = 2(m_w - m_t), \tag{36}$$

where m_w is the mass used in the Wilson-Dirac kernel, and m_t is the Wilson mass at which the smallest eigenvalue is minimum. We use $m_w = 1$ at all simulation points. The values of m_t are listed in the Appendix C.

We compute the correlators of scalar and vector bilinears at zero spatial momentum defined in the continuum by

$$G_\Sigma(t) = \int dxdy \Big\langle \Sigma(x,y,t)\Sigma(0,0,0) \Big\rangle \quad \text{and} \quad G_V(t) = \int dxdy \Big\langle V_i(x,y,t)V_i(0,0,0) \Big\rangle, \tag{37}$$

respectively. On the lattice, after Wick contractions, the correlators using massless fermions become

$$\begin{aligned} G_\Sigma(T) &= \frac{L^2}{\ell^2 Z_m^2} \sum_{X,Y} \text{tr} \left[A(0,0,0;X,Y,T) A(X,Y,T;0,0,0) \right] \qquad \text{and} \\ G_V(T) &= \frac{L^2}{\ell^2} \sum_{i=1}^{2} \sum_{X,Y} \text{tr} \left[\sigma_i A(0,0,0;X,Y,T) \sigma_i A(X,Y,T;0,0,0) \right], \end{aligned} \tag{38}$$

where "tr " denotes the trace over the spin index. One of the fermion bilinear is placed at (0,0,0) and the other at (integer) lattice coordinates (X,Y,T) *i.e.*, $T = tL/\ell$ and so on. The factor Z_m in the scalar propagator takes care of the renormalized scalar operator $Z_m^{-1}\Sigma$. Note that since Σ and V are bosonic, their correlators are periodic functions of T with period L. Therefore, we only show the correlators from $T = 0$ to $T = L/2$ in all the plots in this paper.

IV. MASS ANOMALOUS DIMENSION USING ℓ-SCALING OF LOW-LYING EIGENVALUES

The spectrum of the continuum Dirac operator is discrete in a finite box of size ℓ^3. Labeling the discrete (also known as microscopic) spectrum as $0 < \lambda_1 < \lambda_2 < \ldots$, the behavior of λ_i as a function of ℓ will determine whether there is a bilinear condensate or not. If $\lambda_i \sim \ell^{-3}$, then the density of eigenvalues, $\rho(\lambda)$, in the $\ell \to \infty$ limit will be such that $\rho(0) \neq 0$, resulting in a non-zero bilinear condensate. Numerically, studying the behavior of the microscopic spectrum enables us to directly observe the presence or absence of a bilinear condensate without having to extract the infinite volume value of $\rho(0)$ through an extrapolation from $\rho(\lambda)$ for $\lambda > 0$.

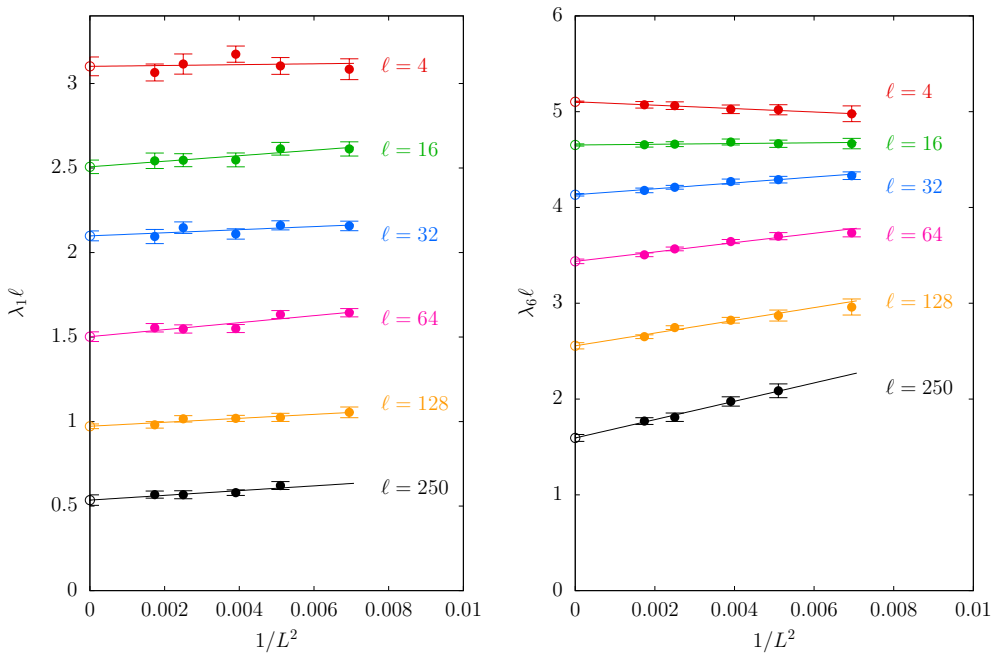

FIG. 1: The dimensionless improved eigenvalues $\lambda_i \ell$ at various ℓ is shown as a function of $1/L^2$ in order to show the remaining dominant $1/L^2$ lattice artifact after the improvement using Z_m. The left and the right panels are for the smallest λ_1 and a larger λ_6 respectively. The data points are from the simulations using $L = 12, 14, 16, 20$ and 24 lattices. The continuum limits are taken using $1/L^2$ extrapolations, which are shown as the straight lines in the plots.

Our previous analysis [29] using massless Wilson fermions provided no evidence for a nonzero bilinear condensate and we found $\lambda_i \sim \ell^{-2}$ for the $N_f = 1$ theory. If we assume

$$\lambda_i \sim \frac{1}{\ell^{1+\gamma_m}}, \tag{39}$$

and find $\gamma_m < 2$, it follows that the γ_m is the mass anomalous dimension since λ_i has the dimensions of mass. In this section, we show that our current simulations with overlap fermions produces results that are quite consistent with our previous studies using massless Wilson fermions for the case of $N_f = 1$.

We show the approach to the continuum limit for the improved first and sixth positive eigenvalues, λ_1 and λ_6, at different fixed ℓ in Figure 1. We find that the leading $\mathcal{O}(1/L)$ lattice corrections are removed by the factor Z_m. Using $1/L^2$ extrapolations, we obtain the continuum limit of the eigenvalues. On the top panel of Figure 2, we show the continuum limit so obtained as a function of ℓ, along with the eigenvalues at finite L. On the bottom panel of Figure 2, we compare the continuum limits obtained using overlap fermions with our earlier result using massless Wilson Dirac operator [29]. A good agreement between the two lattice regularizations

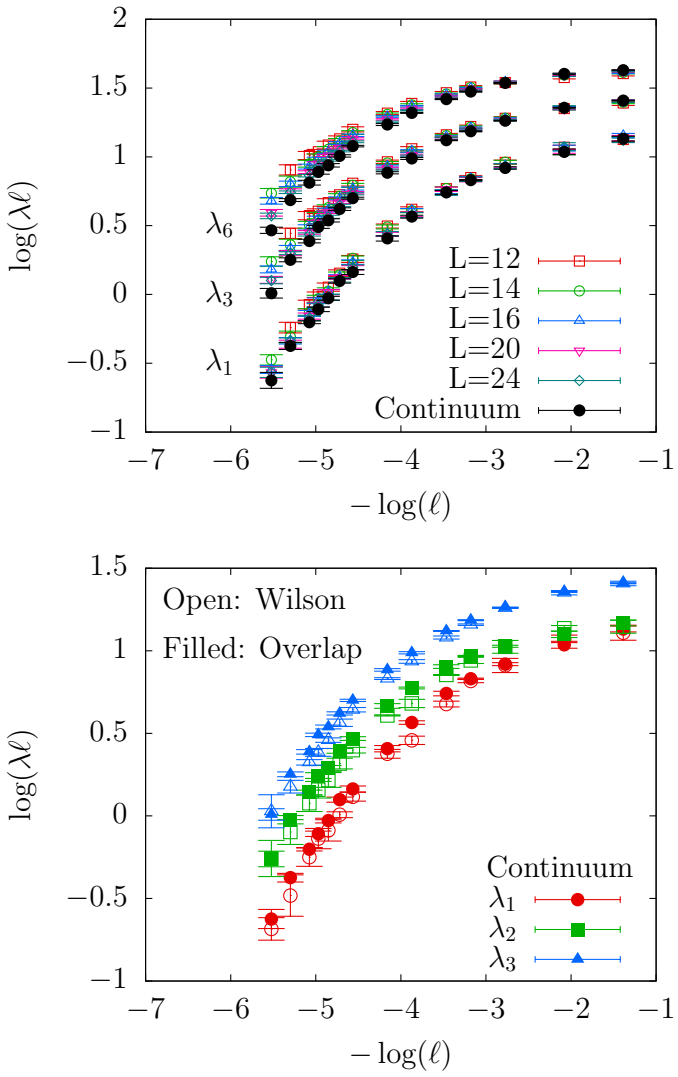

FIG. 2: The top panel shows representative eigenvalues in the continuum along with the ones in finite lattice spacing, as a function of ℓ. On the bottom panel, the continuum limits using overlap (filled symbols) and Wilson-Dirac fermions (open symbols) are compared.

is seen.

We do not find a simple power-law scaling in the region of ℓ where we simulated. We only know the asymptotic dependence of λ on ℓ; we expect the eigenvalues to behave proportional to $\frac{1}{\ell}$ for small ℓ since the theory is asymptotically free, and as $\frac{1}{\ell^{1+\gamma_m}}$ for large ℓ. In order to fit the data over the entire range of ℓ, we found it convenient to parametrize the dependence on ℓ in terms of $\tau = \tanh(1/\ell)$. Since we do not know the functional dependence of λ on ℓ at any intermediary ℓ, we approximate this functional dependence through a rational [1/1] Padé approximant:

$$\lambda\ell = a_1 \tau^{-\gamma_m} \frac{1 + a_2\tau}{1 + a_3\tau}, \tag{40}$$

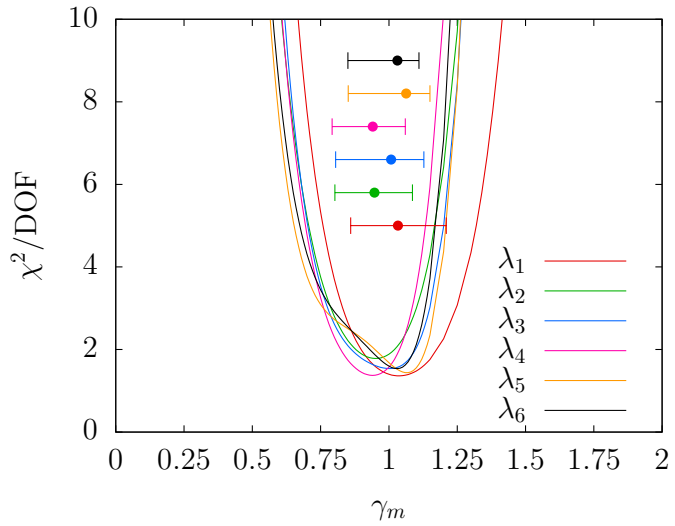

FIG. 3: The χ^2/DOF for the fits using the ansatz in Eq. (40) to the eigenvalue data is shown as a function of the exponent γ_m. These are shown by the colored solid curves for the smallest six eigenvalues. The corresponding 68% confidence interval for the exponent are shown by the error bars.

where the a's are fit parameters. The χ^2/DOF as a function of γ_m is shown in Figure 3. All six low lying eigenvalues predict a value of $\gamma_m = 1.0 \pm 0.2$ with 68% confidence. The fit to the data using $\gamma_m = 1$ is shown in Figure 4.

V. INVERSE PARTICIPATION RATIO AND NUMBER VARIANCE

In the absence of a bilinear condensate, there is no ergodic regime in the eigenvalue spectrum of the massless overlap Dirac operator similar to the observations made about the massless Wilson Dirac operator in [29]. The ergodic regime is characterized by eigenvectors that are completely delocalized and characterized by an IPR defined in Eq. (6) which scales as $I_2 \sim \ell^{-3}$. A complete localization of the eigenvectors will correspond to a value equal to $I_2 = 1$. Instead, we observe a power law behavior with ℓ that is consistent with critical behavior [35–38],

$$I_2 \sim \ell^{-3+\eta}, \tag{41}$$

with $\eta = 0.38(1)$ in the continuum limit as shown in Figure 5. The top panel of Figure 5 shows the finite size scaling of I_2 for the eigenvector corresponding to the smallest eigenvalue, as determined on $L = 24$ lattice. We find IPR to be one of the few observables which show a simple power-law behavior over a range of ℓ we simulated. In the bottom panel, we show the exponent $-3 + \eta$ as a function of $1/L$. The red solid circles are the ones without any improvement, and it shows a leading $\mathcal{O}(1/L)$ lattice correction. The continuum extrapolated value corresponds

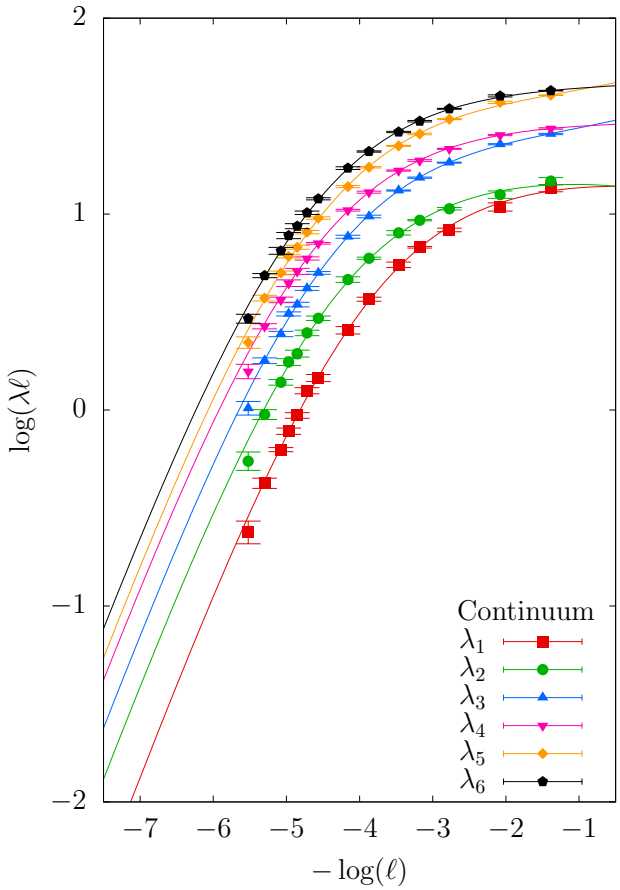

FIG. 4: $\log(\lambda\ell)$ is shown as a function of $-\log(\ell)$ for the smallest six eigenvalues after taking their continuum limits. A power-law $\lambda \sim \ell^{-\gamma_m - 1}$ would be a straight line with a slope γ_m in this plot. No distinct power law is seen in the volumes that we simulated. The ℓ-dependence is well described a [1/1] Padé approximant in Eq. (40) using which we estimate the eventual power-law behavior that would set in at even larger ℓ than we used. The best fits using $\gamma_m = 1$ are shown by the solid curves.

to the one we quoted: $\eta = 0.38(1)$. We empirically find the $\mathcal{O}(1/L)$ to be removed by using an improved definition, I_2/Z_m. These are shown by the blue solid square points, which extrapolates to the same value of η. The black solid diamond data point corresponds to the value as determined using Wilson-Dirac fermions [29]. In Figure 6, we show the exponent $-3+\eta$ for the i-th eigenvector, for different $i = 1, 2, \ldots, 20$. We find the finite-size scaling of IPR to be robust across eigenvectors. The small disagreement in $-3+\eta$ between the overlap and Wilson fermion, is not significant compared to the scatter seen in Figure 6.

If the low-lying eigenvalues are in the critical regime, then we expect the number variance, $\Sigma_2(n)$, to behave linearly with n, with a slope given by $\frac{\eta}{6} = 0.063(3)$. On the left panel of Figure 7, we show the number variance as a function of n at $\ell = 250$ at different L. We do see some

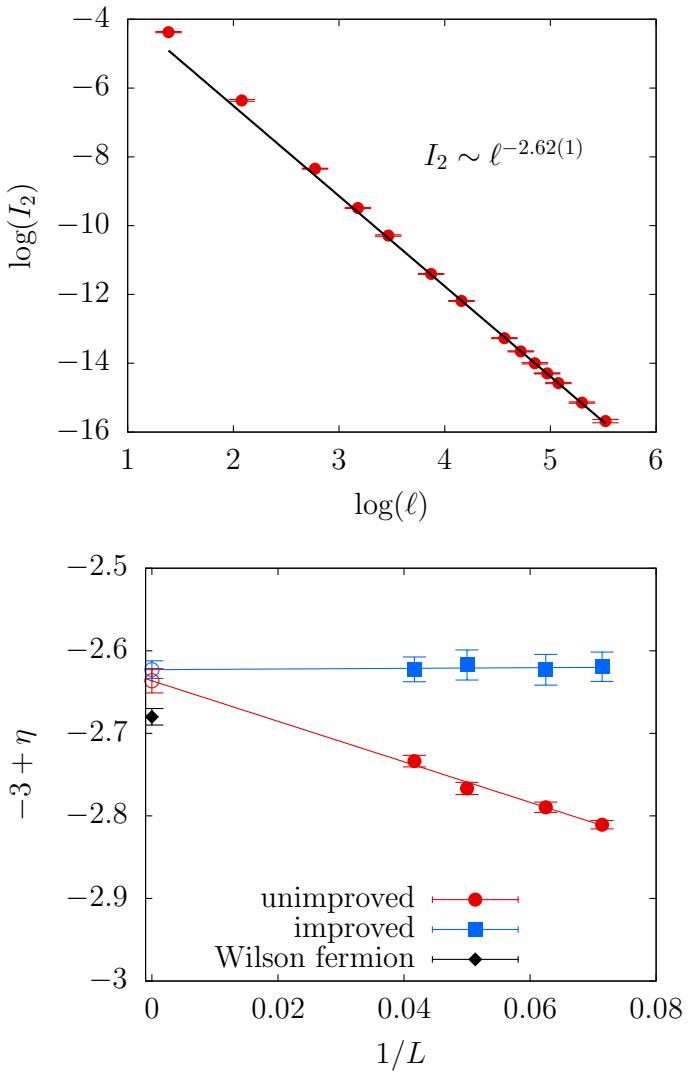

FIG. 5: (top panel) The scaling $I_2 \sim \ell^{-3+\eta}$ is shown using the $L = 24$ data. (Bottom panel) The continuum limit of the exponent $-3+\eta$ using both I_2 (unimproved) and I_2/Z_m (improved) are shown. We estimate $-3+\eta = -2.62(1)$ in the continuum limit. This is close to the value $-2.68(1)$ estimated using Wilson fermions.

finite lattice spacing effects at larger n. The slope of Σ_2 from the finer $L = 24$ lattice matches the critical behavior for a wide range of n. On the right panel of Figure 7, we compare the result from overlap fermion with the one from the Wilson-Dirac fermion [29]. The linear behavior is seen for a wider range with overlap fermions. Perhaps, this is because overlap fermions are exactly massless thereby capturing the fluctuations of the low-lying eigenvalues better than the Wilson-Dirac fermions. Finally, we show the ℓ-dependence of the number variance in Figure 8 where we see that the slope of the linear rise increases with ℓ and approaches the slope $\eta/6$. As we noted in [29], this trend is opposite to the one expected when a condensate is present.

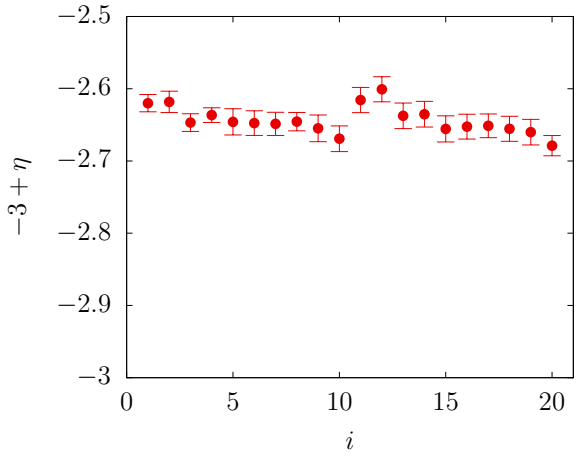

FIG. 6: The exponent $-3+\eta$ for the finite-size scaling of the IPR for various eigenvectors corresponding to the twenty low-lying eigenvalues λ_i.

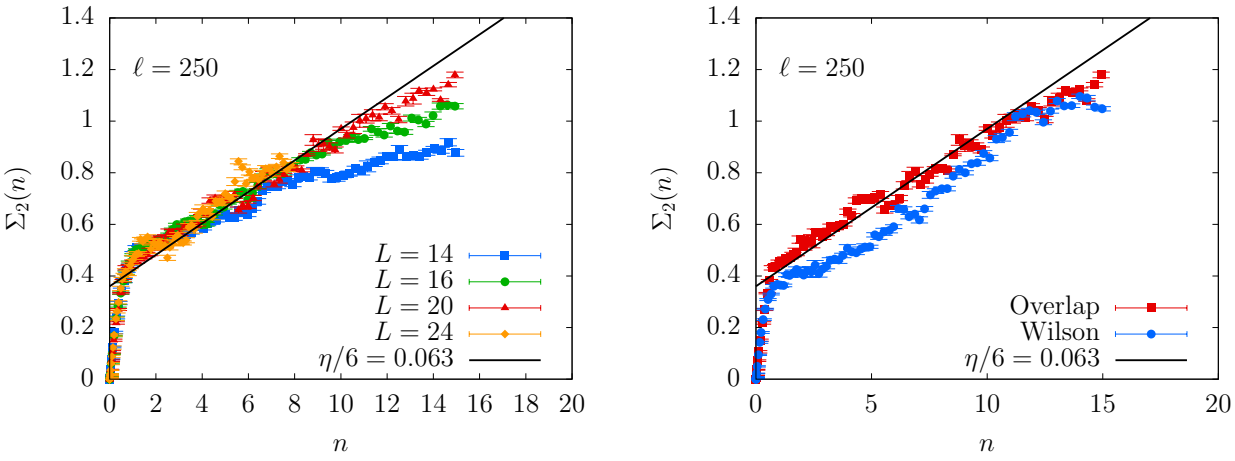

FIG. 7: Lattice spacing effect in number variance. (Left) Number variance $\Sigma_2(n)$ as a function of n is shown for $\ell = 250$ at various lattice sizes L. As lattice spacing is reduced, the number variance at larger n increases and approaches the solid black line which has a slope of $\frac{\eta}{6} = 0.063$. (Right) $\Sigma_2(n)$ for the overlap ($L = 20$) and the Wilson-Dirac fermions ($L = 28$) at $\ell = 250$ are compared.

VI. SCALAR AND VECTOR CORRELATORS

In this section, we study the behavior of the scalar and vector correlators with the aim of lending further support to the scale-invariant nature of the $N_f = 1$ theory. As a start, we attempt to extract a mass using the standard lattice technique [45] of finding the effective mass, $M(t)$, from the zero-spatial momentum correlators $G(t)$. For a correlator in a periodic lattice,

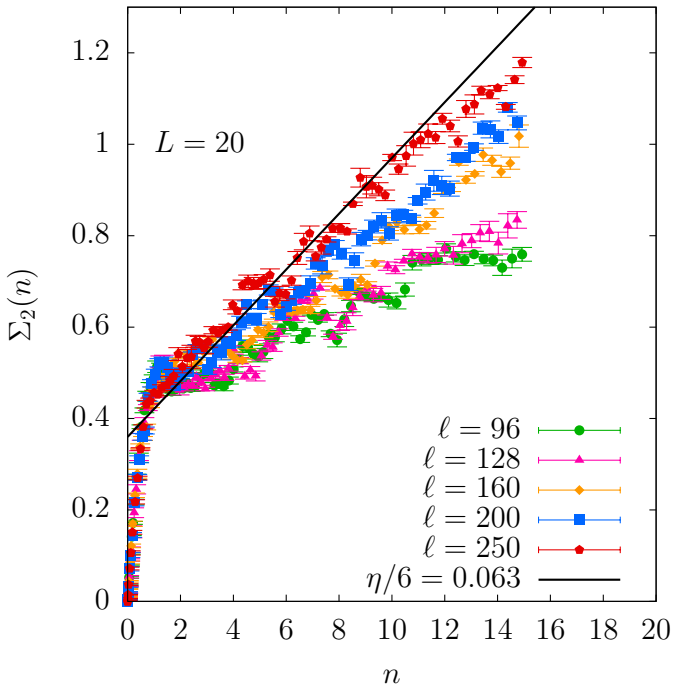

FIG. 8: The number variance is shown as a function of n for various ℓ on $L = 20$ lattice. The black line has a slope of $\frac{\eta}{6} = 0.063$. The slope of the number variance increases with ℓ and approaches $\eta/6$ which is a trend opposite of that expected when a bilinear condensate is present.

one defines the effective mass $M(t)$ using

$$\frac{\cosh\left[M(t)\left(\frac{\ell}{2} - t - \frac{\ell}{L}\right)\right]}{\cosh\left[M(t)\left(\frac{\ell}{2} - t\right)\right]} = \frac{G\left(t + \frac{\ell}{L}\right)}{G\left(t\right)}. \tag{42}$$

If the solution, $M(t)$, to the above equation becomes essentially independent of t for $0 << t \leq \frac{\ell}{2}$, then this t-independent value, M, can be used as an upper bound to the lowest state that contributes to the correlator, $G(t)$. The results for the scalar and vector effective masses are shown in Figure 9. One should note that we have plotted the effective mass times the box size, $M(t)\ell$, on the y-axis. There is reasonable evidence for $M(t)\ell$ approaching a limit for large t. A striking observation is that $M\ell$ is essentially independent of the box size ℓ. This indicates that the upper bound on the mass M in physical units approaches zero in the infinite volume limit for both the scalar and vector correlators [2]. Therefore, there is no mass gap in these two sectors of the theory. One could take the point of view that the value of M in the plateau of the effective mass plot is actually a mass gap at finite ℓ. In such a case, $M \sim \ell^{-1}$ behavior

[2] A fit to both the scalar and vector correlators with two massive states resulted in both of the masses approaching zero in the infinite volume.

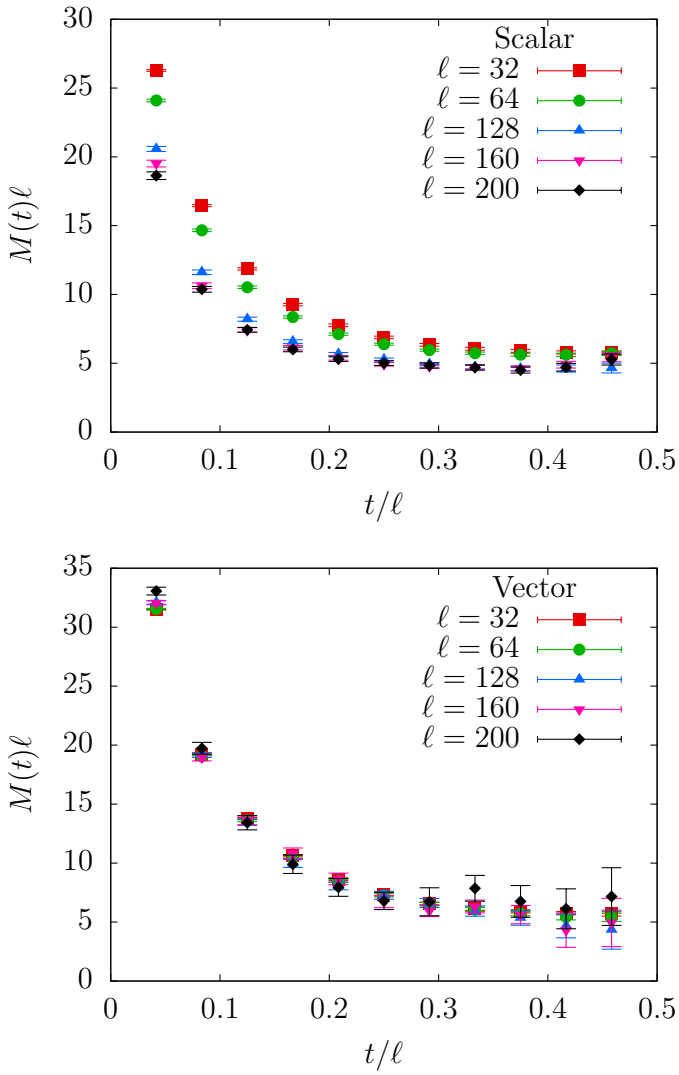

FIG. 9: The figure shows the dimensionless effective mass $M(t)\ell$ as a function of $\frac{t}{\ell}$ for different ℓ, represented by different colored symbols. The top and the bottom panels are for the scalar and vector respectively, as determined on $L = 24$ lattice. The value of $M\ell$ along the plateau seen in both the panels gives an upper bound on the mass gap (times ℓ) present in the scalar and vector correlators. Since the position of plateau seems to be independent of ℓ, $M \sim 1/\ell$.

could be explained as the standard hyper-scaling relation for a scale-invariant theory. As for a larger conformal invariance is concerned, such a mass gap could arise by the explicit breaking of conformal symmetry by the finite box size, as shown in two-dimensions [46].

Next, we look at the correlators themselves to see evidence for a power-law behavior. First, we show that the lattice spacing effects in the scalar and vector correlators are under control in Figure 10; the top panels show the vector correlator at different L on two box sizes representative of small and large ℓ. Similar plots for the scalar are shown in the bottom panels.

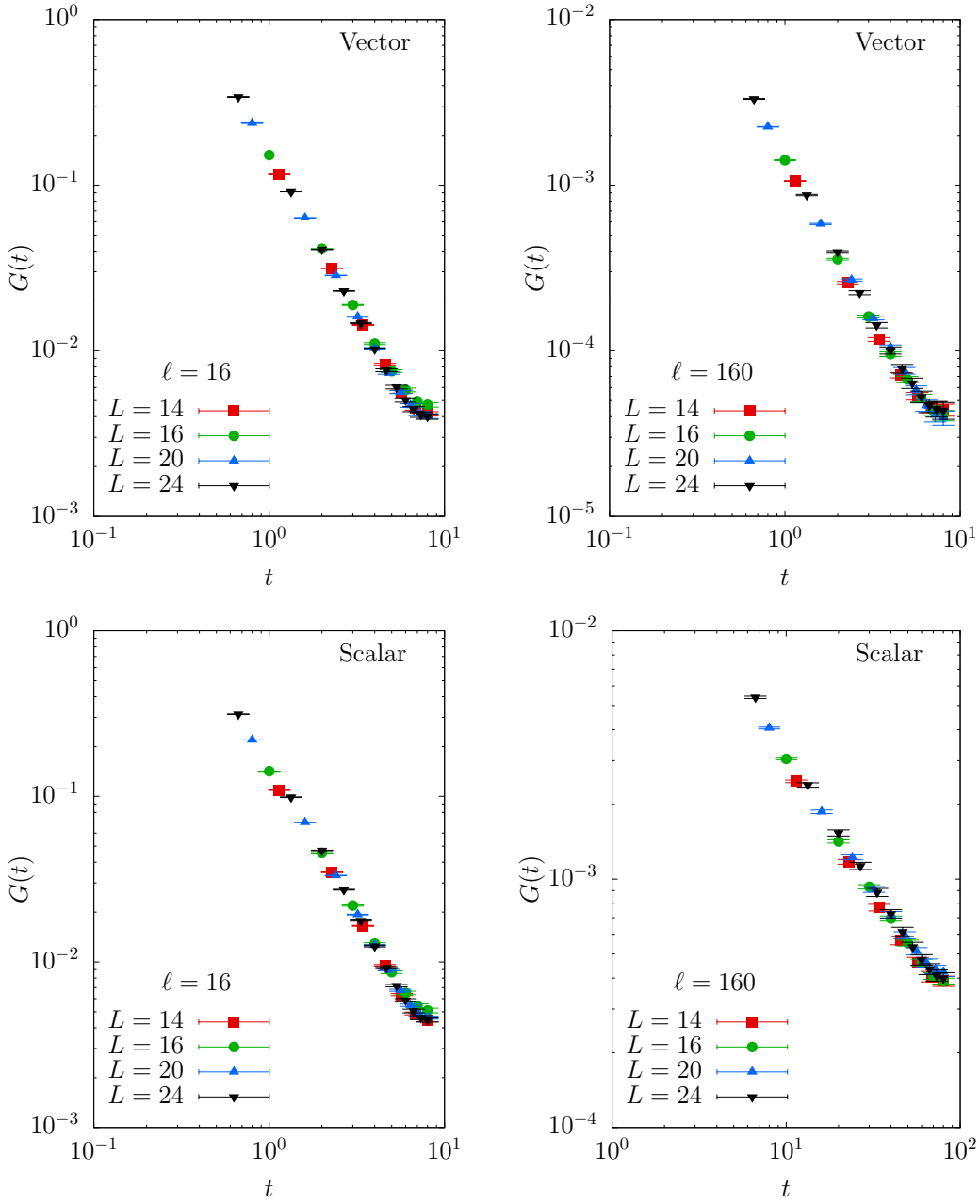

FIG. 10: Small lattice spacing effects in the correlators. The zero spatial momentum correlators $G(t)$ are plotted as a function of physical separation t. The top panels are for the vector and the bottom ones for the scalar. The different colored symbols denote the different L^3 lattices used to determine the correlators at fixed ℓ. Lattice effects are small in both finer ($\ell = 16$ on the left panels) and coarser ($\ell = 160$ on the right panels) lattices.

The brute force way to obtain the correlators at infinite volume is to take the $L \to \infty$ limit of the correlators at each ℓ, and then take $\ell \to \infty$ at each physical t. Such a procedure is not numerically feasible. Since the lattice artifacts in the correlators are under control, we can

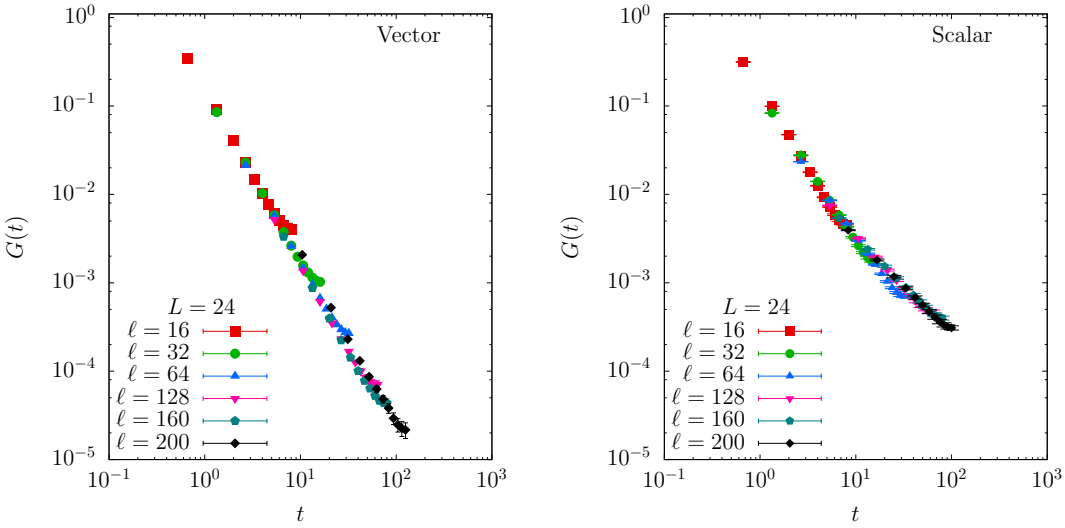

FIG. 11: The figures show the vector and scalar correlators G as a function of physical separation t, by putting together the data from various ℓ, on $L = 24$ lattice. The different colored symbols correspond to various representative ℓ. (Left) Vector shows a power-law behavior as a function of t. The small deviations are due to effect of periodicity at finite ℓ. (Right) Scalar does not show a simple power-law, nevertheless massless, as seen by the concave-up nature of the correlator in the log-log plot.

use the correlators determined at different ℓ on the same L^3 lattice to scan a wide range of physical t. This is possible provided the ℓ dependence of the correlators at fixed t are small. Such a reconstruction of infinite volume correlators for the scalar and vector over a range of t covering three orders of magnitude are shown in Figure 11. We do see a clear approach to the infinite volume limit at a fixed t, after the fact. The vector correlator shows a clean power law behavior, while the scalar does not. However, the scalar correlator in the log-log plot in Figure 11 is concave up, which again rules out the presence of a mass gap because an exponential on a log-log plot is concave down. Thus, we are left with the possibility that the leading scaling behavior for the scalar would set in at even larger values of physical t.

Before we further explore the possible power-law behavior at larger separations t, we digress to consider the expected behavior of the zero spatial momentum correlator of a primary operator in a conformal field theory. Consider the power-law correlation function,

$$G_\Delta(x, y, t) \propto \frac{1}{(x^2 + y^2 + t^2)^\Delta}, \tag{43}$$

corresponding to a primary operator of conformal dimension Δ in a CFT. Its zero momentum correlation function will behave as

$$G_\Delta(t) = \int dxdy\; G_\Delta(x, y, t) \propto \frac{1}{t^k} \qquad \text{where} \qquad k = 2(\Delta - 1). \tag{44}$$

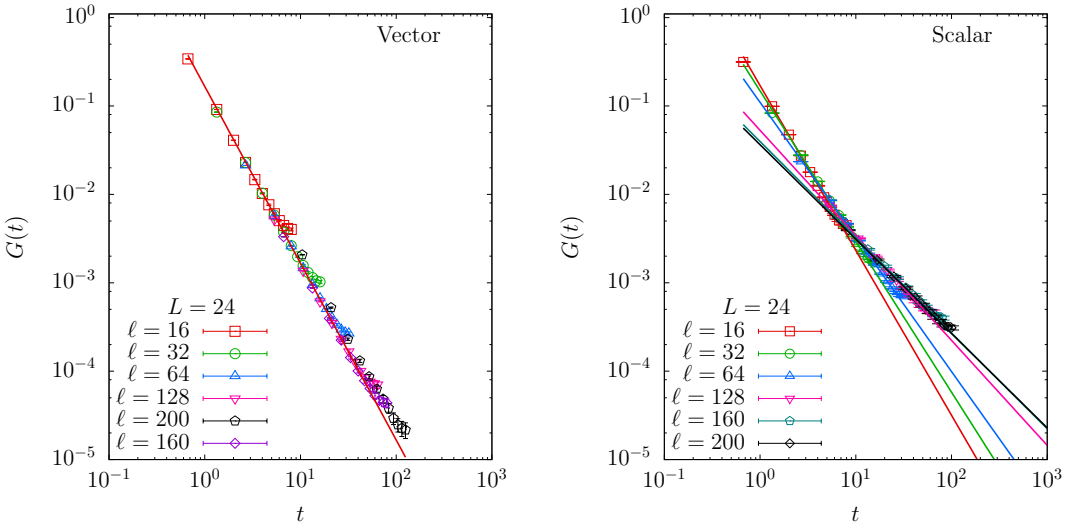

FIG. 12: The tangents, which have a slope $d\log(G)/d\log(t)$, are shown along with the correlator data, same as the ones shown in Figure 11. On the left panel, the red solid line corresponds to a t^{-2} power-law. On the right panel, the different colored lines are the tangents determined at various $t = t_o(\ell) \equiv \ell/L$ using the finite-ℓ scalar correlator data on $L = 24$ lattice, which are represented by symbols of the same color.

Both the scalar and vector bilinears have an engineering mass dimension equal to 2. Since the vector bilinear is associated with a conserved current, it will not acquire any anomalous dimension. Therefore, $\Delta_V = 2$, and we should find

$$G_V(t) \propto \frac{1}{t^2}. \tag{45}$$

Since mass acquires an anomalous dimension $1 + \gamma_m$, the scalar bilinear will also acquire an anomalous dimension such that the sum of the dimensions is equal to 3. Therefore

$$\Delta_\Sigma = 2 - \gamma_m. \tag{46}$$

We have shown in the previous section that $\gamma_m = 1.0 \pm 0.2$, which along with Eq. (44) and Eq. (46), suggests that

$$\Delta_\Sigma = 1.0 \pm 0.2 \qquad \text{and} \qquad G_\Sigma(t) \propto \frac{1}{t^{0.0\pm0.4}}. \tag{47}$$

Since the correlator has to vanish as $t \to \infty$, we see that $\gamma_m = 1.0$ is marginal for power law behavior which also follows from unitarity constraints in CFTs [34].

The vector correlator is shown on the left panel of Figure 12. It exhibits a clear power-law behavior over the entire range of the plot — $G(t) \sim t^{-2}$ (shown as a red solid line in Figure 12) describes the data well. Thus the vector indeed does not get an anomalous dimension. This

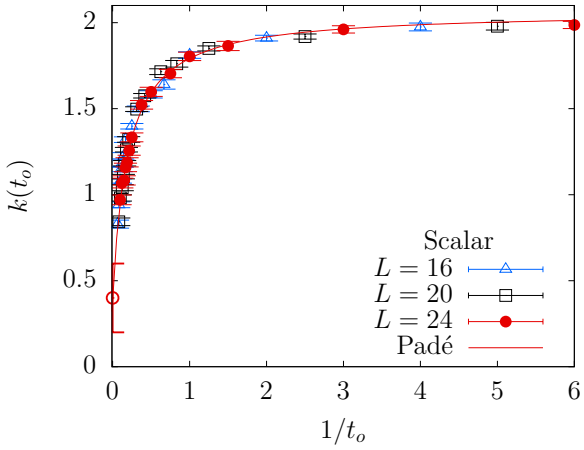

FIG. 13: The scale-dependent exponent $k(t)$ for the scalar. The figure shows the behavior of $k(t_o)$ defined as $d\log\left(G(t)\right)/d\log(t)$ determined at various $t = t_o(\ell) \equiv \ell/L$ using the various finite-ℓ scalar correlator data. The different colored symbols correspond to different L. At smaller t_o, the value of k seems to flow to 2. At larger t_o, it keeps decreasing and the value it approaches as $t_o \to \infty$ is the power-law exponent corresponding to the infra-red fixed point. By using a [1/1] Padé in $\tanh(1/t_o)$, shown by the red solid line, we estimate the infinite t limit of k to be 0.4(2). This corresponds to a mass anomalous dimension $\gamma_m = 0.8(1)$.

might be non-trivial in light of Ref [47] which was used recently in [48] to argue for a possible phase with spontaneously broken Lorentz symmetry.

The scalar correlator is shown on the the right panel of Figure 12. It does not show a simple power law behavior over the entire range. In particular, the behavior at small t is quite different from the behavior at large t. In order to estimate the asymptotic behavior, we use the following strategy. We numerically estimate the tangent, $k(t)$, on the log-log plot at various values of t. We have already shown that the $L = 24$ data can be assumed to be the continuum result to a good accuracy. In any region of t in Figure 12, data from multiple ℓ overlap. Given a fixed value of ℓ, we have a set of $t_n = \frac{\ell(n+1)}{L}$ values that appear on the plot. We use $n = 0, 1, 2, \ldots, L/4$ and fit a straight line to the data at a fixed ℓ and call that as the tangent, $k(t_0)$. These are the various colored lines in Figure 12 that correspond to tangents determined using the correlator data from ℓ, represented by the same color.

In Figure 13, we show this slope k as a function of t_o. We confirm our earlier statement that the $L = 24$ data describes the continuum quite well by showing that the results from three different lattice spacings lie on the same curve. The short-distance behavior of the correlator is governed by an exponent $k = 2$. As t is increased, the exponent decreases. One could interpret

this as a flow from the trivial UV fixed point into a non-trivial infra-red fixed point as the length-scale t is increased. Equivalently, the bilinear scalar operator is not a simple primary operator in a conformal field theory but one primary operator dominates the long distance behavior. Using a [1/1] Padé approximant in $\tanh(1/t_o)$, we extrapolate $k(t)$ to its $t \to \infty$ infra-red value. We estimate $k(\infty) = 0.4(2)$. This corresponds to an estimate of the anomalous dimension of mass from the scalar correlator, $\gamma_m = 0.8(1)$. This is in good agreement with the one obtained in Section IV. Our estimate of the mass anomalous dimension from the correlator excludes $\gamma_m = 1$ since the correlator approaches zero as $t \to \infty$.

VII. CONCLUSIONS

We have performed a numerical investigation of three dimensional QED coupled to two flavors of two-component massless fermions while preserving parity. We used overlap fermion which preserves the full U(2) symmetry away from the continuum limit. We extracted physical quantities on a three-dimensional continuum torus of size ℓ^3 by studying the continuum limit at a fixed ℓ. By studying the finite-size scaling of the low-lying eigenvalues of the massless anti-Hermitian overlap Dirac operator, we confirmed the absence of a bilinear condensate that was previously established using Wilson-Dirac fermions [29]. This enabled us to obtain a value for the mass anomalous dimension, namely, $\gamma_m = 1.0 \pm 0.2$, which is at the upper edge of the allowed value for a conformal field theory. The eigenvectors associated with the low lying eigenvalues of the anti-Hermitian overlap Dirac operator showed critical behavior in the sense of a metal-insulator transition. The scaling behavior of the inverse participation ratio (IPR) of the associated eigenvectors and the linear behavior of number variance of the low lying eigenvalues were consistent with critical behavior. Our analysis of the scalar and vector correlators showed that there is no mass gap in these sectors of the theory. The power law behavior of the vector correlator was consistent with the vector current being conserved. The asymptotic power law behavior of the scalar correlator resulted in an independent estimate of the mass anomalous dimension, namely, $\gamma_m = 0.8(1)$.

The analysis performed in this paper along with the results in [29] suggests that three dimensional QED with $2N_f$ number of two component massless fermions is scale invariant for $N_f \geq 1$ when ones uses a regularization that preserves parity. In order to consider theories where one has a phase where scale invariance is broken, we plan to extend our studies to non-abelian gauge theories in three dimensions. As a start, we are currently studying three-dimensional SU(N) gauge theories in the large N limit where fermions are quenched, provided

parity is preserved. Preliminary numerical studies [49] suggest that there is a non-zero bilinear condensate in this limit. The natural direction we plan to pursue is to map out the phase transition in the N-N_f plane that separates a scale invariant phase from one where there is a bilinear condensate. Another direction we plan to pursue is to consider U(1) gauge fields in four dimensions coupled to fermions in three dimensions. The extent of the fourth direction changes the gauge action from the limit considered in this paper where the extent of the fourth direction was set to zero. This is in the spirit of what one is interested in condensed matter physics and it is possible that scale invariance is broken if the fourth direction is large enough. We also plan to perform numerical studies in this direction.

Acknowledgments

All computations in this paper were made on the JLAB computing clusters under a class B project. The authors acknowledge partial support by the NSF under grant number PHY-1205396 and PHY-1515446. We thank Dam Son and Igor Klebanov for useful discussions.

Appendix A: Generating functional

We develop the basic formula for the generating function following [39]. Although the technical details are not new, the final result shows the explicit form of the propagator for a two-component fermion. Let

$$Z(\eta,\bar{\eta}) = \langle 0- | \exp\left[\bar{\eta} b + a^\dagger \eta\right] |0+\rangle. \tag{A1}$$

We define new sets of creation operators as

$$r_+^\dagger = a^\dagger \frac{1+V}{2}\mathcal{R} + b^\dagger \frac{1-V}{2}\mathcal{R}; \qquad l_-^\dagger = b^\dagger \mathcal{R}, \tag{A2}$$

and new sets of annihilation operators as

$$l_+ = \mathcal{R}^\dagger \frac{1-V^\dagger}{2} a + \mathcal{R}^\dagger \frac{1+V^\dagger}{2} b; \qquad r_- = \mathcal{R}^\dagger a. \tag{A3}$$

It follows from Eq. (19) and Eq. (20) that

$$r_+^\dagger |0+\rangle = 0; \qquad l_+ |0+\rangle = 0; \qquad \langle 0- | r_- = 0; \qquad \langle 0- | l_-^\dagger = 0. \tag{A4}$$

Inverting Eq. (A2) and Eq. (A3), we arrive at

$$b^\dagger = l_-^\dagger \mathcal{R}^\dagger; \qquad a^\dagger = r_+^\dagger \mathcal{R}^\dagger \frac{2}{1+V} - l_-^\dagger \mathcal{R}^\dagger A; \tag{A5}$$

and

$$a = \mathcal{R} r_-; \qquad b = \frac{2}{1+V^\dagger}\mathcal{R} l_+ + A\mathcal{R} r_-. \tag{A6}$$

Using the above equations, we can write

$$\bar{\eta} b + a^\dagger \eta = Q_+ + Q_-, \tag{A7}$$

where

$$Q_+ = r_+^\dagger \mathcal{R}^\dagger \frac{2}{1+V}\eta + \bar{\eta}\frac{2}{1+V^\dagger}\mathcal{R} l_+; \qquad Q_- = \bar{\eta} A \mathcal{R} r_- - l_-^\dagger \mathcal{R}^\dagger A \eta. \tag{A8}$$

This split is equivalent to

$$Q_+ = a^\dagger \eta + b^\dagger A \eta - \bar{\eta} A a + \bar{\eta} b; \qquad Q_- = -b^\dagger A \eta + \bar{\eta} A a. \tag{A9}$$

From the canonical anti-commutation relations, it follows that

$$[Q_+, Q_-] = -2\bar{\eta} A \eta. \tag{A10}$$

Therefore, we have

$$\begin{aligned} Z(\eta, \bar{\eta}) &= \langle 0- | \exp[Q_+ + Q_-] |0+\rangle \\ &= \exp\left(\frac{1}{2}[Q_+, Q_-]\right) \langle 0- | e^{Q_-} e^{Q_+} |0+\rangle \\ &= \exp\left(\frac{1}{2}[Q_+, Q_-]\right) \langle 0- |0+\rangle \\ &= \exp[-\bar{\eta} A \eta] \det \frac{1+V}{2}. \end{aligned} \tag{A11}$$

This result will be used in Appendix B.

Appendix B: Introduction of parity invariant mass terms

The partition function for the $N_f = 1$ parity-invariant theory with massless fermions is

$$Z_2 = \big\{ {}_1\langle 0- | \otimes {}_2\langle 0+ | \big\} \big\{ |0+\rangle_1 \otimes |0-\rangle_2 \big\}. \tag{B1}$$

Parity invariance is ensured by $Z_2 \to Z_2^*$ and $1 \leftrightarrow 2$. The generating functional for $N_f = 1$ theory with parity invariant mass terms is

$$\begin{aligned} Z_2(\eta_1, \eta_2, \bar{\eta}_1, \bar{\eta}_2; m_1, m_2, m_3) &= {}_1\langle 0- | \otimes {}_2\langle 0+ | \\ &\exp\left[\bar{\eta}_1 b_1 + a_1^\dagger \eta_1 - \bar{\eta}_2 a_2 + b_2^\dagger \eta_2 + m_1 a_1^\dagger b_1 + m_1 b_2^\dagger a_2 + m_2 a_1^\dagger a_2 + m_3 b_2^\dagger b_1\right] \\ &|0+\rangle_1 \otimes |0-\rangle_2. \end{aligned} \tag{B2}$$

Using standard manipulations of converting the mass terms bilinear in creation-annihilation operators by introducing auxiliary Grassmann fields, and then using the result from Appendix A, the final result is

$$Z_2(\eta_1,\eta_2,\bar{\eta}_1,\bar{\eta}_2;m_1,m_2,m_3) \;=\; \det\frac{1+V}{2}\det\frac{1+V^\dagger}{2}\det\left[(1+m_1A)(1-m_1A)+m_2m_3A^2\right] \\ \exp\left[-\begin{pmatrix}\bar{\eta}_1 & \bar{\eta}_2\end{pmatrix}\frac{\left[A\mathbb{I}+A^2\begin{pmatrix}-m_1 & m_2\\ -m_3 & m_1\end{pmatrix}\right]}{(1+m_1A)(1-m_1A)+m_2m_3A^2}\begin{pmatrix}\eta_1\\ \eta_2\end{pmatrix}\right]. \tag{B3}$$

We proceed to go to a flavor diagonal basis by diagonalizing the mass matrix using

$$W=\begin{pmatrix}m_1+m & m_2\\ m_3 & m+m_1\end{pmatrix}. \tag{B4}$$

where

$$m=\sqrt{m_1^2-m_2m_3}. \tag{B5}$$

The matrix, W, is invertible as long as $m_1^2\neq m_2m_3$ and $m_1\neq -1$. Defining flavor diagonal sources as

$$\begin{pmatrix}\bar{\eta}_+ & \bar{\eta}_-\end{pmatrix}=\begin{pmatrix}\bar{\eta}_1 & \bar{\eta}_2\end{pmatrix}W;\qquad \begin{pmatrix}\eta_+\\ \eta_-\end{pmatrix}=W^{-1}\begin{pmatrix}\eta_1\\ \eta_2\end{pmatrix}, \tag{B6}$$

and noting that

$$(1+mA)(1-mA)=(1+m_1A)(1-m_1A)+m_2m_3A^2, \tag{B7}$$

we arrive at Eq. (24).

Appendix C: Simulation details

We generated gauge-field configurations using two flavors of dynamical massless overlap fermions in three-dimensional torus with different physical extents ℓ using L^3 lattices. The parameters ℓ and L enter the lattice coupling of the non-compact gauge action:

$$S_g=\frac{L}{\ell}\sum_n\sum_{j<k}^{3}\left[\theta_j(n)+\theta_k(n+\hat{j})-\theta_j(n+\hat{k})-\theta_k(n)\right]^2, \tag{C1}$$

where θ's are related to the physical gauge-fields A_k as $\theta_k=\frac{\ell}{L}A_k$. We tabulate the set of ℓ and L used in this study in Table I. We used the Sheikhoslami-Wohlert-Wilson-Dirac operator [50], adapted to three-dimensions in [29], as the kernel X for the overlap Dirac operator.

ℓ	m_t				
	$L=12$	$L=14$	$L=16$	$L=20$	$L=24$
4	0.032(12)	0.02233(90)	0.0182(62)	0.0091(48)	0.0067(30)
8	0.029(10)	0.0178(87)	0.0145(72)	0.0085(41)	0.0041(31)
16	0.028(11)	0.0186(67)	0.0133(49)	0.0055(32)	0.0022(21)
24	0.0326(84)	0.0185(60)	0.0137(46)	0.0068(23)	0.0033(21)
32	0.0435(81)	0.0299(71)	0.0222(40)	0.0126(19)	0.0053(20)
48	0.072(18)	0.0542(62)	0.0396(48)	0.0244(36)	0.0145(16)
64	0.104(10)	0.0750(85)	0.0635(45)	0.0401(37)	0.0267(21)
96	0.164(15)	0.133(12)	0.1123(75)	0.0790(52)	0.0574(38)
112	0.204(17)	0.165(15)	0.1337(85)	0.0996(62)	0.0747(37)
128	0.229(22)	0.193(16)	0.1633(86)	0.1181(53)	0.0917(47)
144	0.255(12)	0.221(17)	0.183(12)	0.1396(91)	0.1084(52)
160	0.268(21)	0.242(19)	0.207(14)	0.1605(78)	0.1264(65)
200	0.323(25)	0.308(28)	0.254(14)	0.206(13)	0.1659(66)
250	0.453(30)	0.334(23)	0.297(17)	0.270(16)	0.214(12)

TABLE I: The list of tuned Wilson mass m_t, which minimizes the lowest eigenvalue of the Wilson-Dirac operator, for various physical length of the torus ℓ and lattice sizes L used in this study.

As explained in [29], we improved the Sheikhoslami-Wohlert-Wilson-Dirac operator by using one-level HYP smeared θ's in the fermion action [51, 52]. We used the optimal smearing parameters $s_1 = 0.6$ and $s_2 = 0.5$. Smearing is essential in our study to explore a range of ℓ without the exorbitant computational cost of using very large L. One can see this by considering the monopole density ρ_m at finite value of L. In a non-compact U(1) theory, monopoles are not physical since they are infinite energy objects, hence they are lattice artifacts. We determined ρ_m for unsmeared as well as optimal HYP smeared gauge-fields using the procedure outlined in [53]. On the left panel of Figure 14, we show that the monopole density in the unsmeared gauge-field indeed increases with ℓ at any finite L. At the same time, we also check that the monopole density vanishes in the continuum limit $L \to \infty$ at all ℓ. One could have avoided using smearing, but lattice artifacts would have been large in the values of L we simulated. On the right panel, we show a similar plot for optimal HYP smeared gauge fields. Now, we find that even with one-level of smearing, monopoles are completely removed at all ℓ. Since the fermions

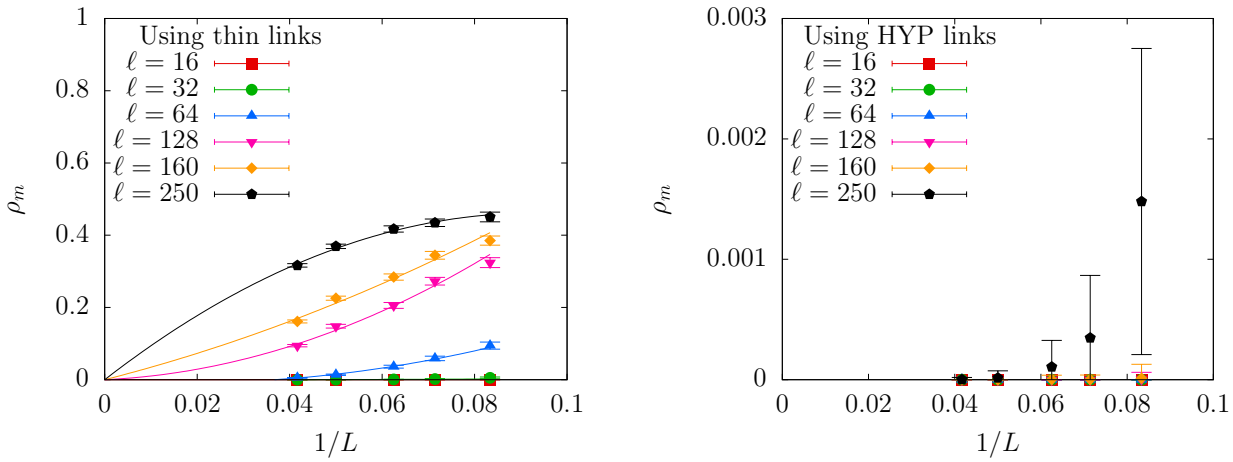

FIG. 14: The monopole density ρ_m at various ℓ as the continuum limit is approached by taking $L \to \infty$. The left panel shows the result for the unsmeared, thin gauge-links. The solid lines show how the density approaches zero using a quadratic $1/L$ extrapolation. On the the right panel, the result when optimal HYP smearing is used is shown. With this improvement, the monopole density is consistent with zero at all simulation points.

see only the smeared gauge-fields, it explains why the fermionic observables exhibit small lattice spacing effects. In addition to removing monopole-like defects, smearing also results in a well-defined value of m_t where the smallest eigenvalue of the Sheikhoslami-Wohlert-Wilson-Dirac operator is minimum. We tabulate the values of m_t, which we use to find the normalization factor Z_m (refer Eq. (36)), in Table I.

We tuned the step-size for the leap-frog evolution at run-time such that acceptance was at least 80%. As for the statistics, we generated $13,000$ to $14,000$ trajectories at each simulation point. Then we used only configurations separated by an auto-correlation time, as determined from the smallest eigenvalue Λ_1. This amounted to 500 to 1000 independent configurations at all the simulation points.

Appendix D: HMC force calculation

In this section, we derive the expression for the fermionic HMC force for the case of $N_f = 1$ massless overlap fermions. The fermion force from the pseudo-fermion action in Eq. (35) is

$$F_\mu(x) = -\frac{\partial S_f}{\partial \theta_\mu(x)} = -\phi^\dagger \frac{\partial \left(C_o^\dagger C_o\right)^{-1}}{\partial \theta_\mu(x)} \phi, \tag{D1}$$

where the link variable is $U_\mu(x) = e^{i\theta_\mu(x)}$ as defined in [29] using the non-compact gauge field. The fermion force when a smeared gauge-link is used in the fermion action, as done in this

paper, is obtained by the standard chain-rule, as explicitly worked out in [29].

Let us define

$$\Psi \equiv \left(C_o^\dagger C_o\right)^{-1} \phi. \tag{D2}$$

Then

$$F_\mu(x) = \Psi^\dagger \frac{\partial C_o^\dagger C_o}{\partial \theta_\mu(x)} \Psi. \tag{D3}$$

We use Eq. (33) and $VV^\dagger = 1$ to write Eq. (D3) as

$$F_\mu(x) = -\frac{1}{2}\mathrm{Re}\left(\Psi^\dagger V' \Psi\right); \quad V' = \frac{\partial V}{\partial \theta_\mu(x)}. \tag{D4}$$

V can be computed approximately using

$$V = X \sum_{k=1}^{n} \frac{r_k}{X^\dagger X + p_k}. \tag{D5}$$

We use $n = 21$ in our computations. Defining

$$Y_k \equiv \frac{1}{X^\dagger X + p_k} X^\dagger \Psi; \quad Z_k \equiv \frac{r_k}{X^\dagger X + p_k} \Psi; \quad \tilde{Y}_k \equiv X Y_k; \quad \tilde{Z}_k \equiv X Z_k, \tag{D6}$$

the fermion force becomes

$$F_\mu(x) = -\frac{1}{2}\mathrm{Re}\left\{ \Psi^\dagger X' \left(\sum_{k=1}^{n} Z_k \right) - \sum_{k=1}^{n} \left(\tilde{Y}_k^\dagger X' Z_k + \tilde{Z}_k^\dagger X' Y_k \right) \right\}, \tag{D7}$$

where

$$X' = \frac{\partial X}{\partial \theta_\mu(x)}. \tag{D8}$$

As explained in Appendix C, we used Sheikhoslami-Wohlert-Wilson-Dirac operator in place of the unimproved Wilson Dirac operator, X.

As is well known, there are two kinds of inversions that enter the dynamical overlap simulation — the ones that require the multiple shifted inversion of $X^\dagger X$ which we refer to as "inner CG", and the inversion of $C_o^\dagger C_o$ which we call the "outer CG", and it again involves a nested inner CG. We use a stopping criterion that the ratio of the norm of the residue to the norm of the solution vector to be less than ϵ. For the inversions required along the molecular dynamics trajectory, we used a stopping criterion $\epsilon_{\mathrm{in}} = 10^{-6}$ for the inner CG, and a stopping criterion $\epsilon_{\mathrm{out}} = 10^{-4}$ for the outer CG. We used a more stringent stopping criterion of $\epsilon_{\mathrm{in}} = 10^{-8}$ and $\epsilon_{\mathrm{out}} = 10^{-6}$ for the inversions required in the computation of fermion action used in the accept-reject step. In Figure 15, we compare the run-time histories of the smallest eigenvalue of the overlap operator at $\ell = 160$ on $L = 14$ lattice. Using a starting thermalized configuration, one

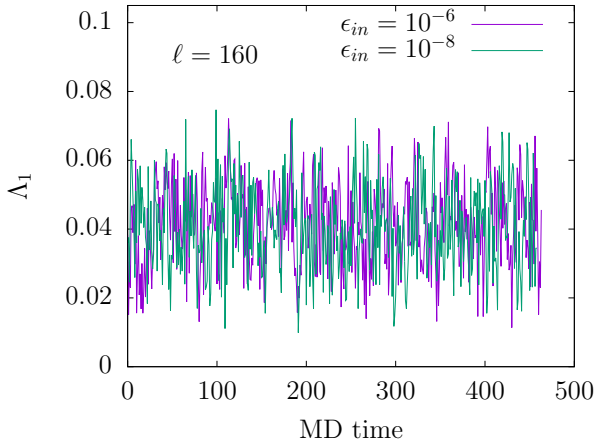

FIG. 15: Run-time history of the lowest eigenvalue using two different stopping criterion for the inner CG, $\epsilon_{\rm in} = 10^{-6}$ and 10^{-8}. The corresponding stopping criterion for the outer CG were $100\epsilon_{\rm in}$.

of the runs was made using $(\epsilon_{\rm in} = 10^{-6}, \epsilon_{\rm out} = 10^{-4})$ and another with $(\epsilon_{\rm in} = 10^{-8}, \epsilon_{\rm out} = 10^{-6})$. We find that it is sufficient to use the less stringent stopping criterion.

---

[1] S. Deser, R. Jackiw, and S. Templeton, Annals Phys. **140**, 372 (1982).

[2] S. Deser, R. Jackiw, and S. Templeton, Phys.Rev.Lett. **48**, 975 (1982).

[3] A. Redlich, Phys.Rev. **D29**, 2366 (1984).

[4] A. Niemi and G. Semenoff, Phys.Rev.Lett. **51**, 2077 (1983).

[5] G. W. Semenoff, Phys. Rev. Lett. **53**, 2449 (1984).

[6] N. Seiberg, T. Senthil, C. Wang, and E. Witten (2016), 1606.01989.

[7] A. Karch and D. Tong (2016), 1606.01893.

[8] V. A. Miransky and I. A. Shovkovy, Phys. Rept. **576**, 1 (2015), 1503.00732.

[9] A. H. Castro Neto, F. Guinea, N. M. R. Peres, K. S. Novoselov, and A. K. Geim, Rev. Mod. Phys. **81**, 109 (2009).

[10] M. Franz, Z. Tesanovic, and O. Vafek, Phys. Rev. **B66**, 054535 (2002), cond-mat/0203333.

[11] I. F. Herbut, Phys. Rev. **B66**, 094504 (2002), cond-mat/0202491.

[12] R. D. Pisarski, Phys.Rev. **D29**, 2423 (1984).

[13] T. Appelquist, M. J. Bowick, E. Cohler, and L. C. R. Wijewardhana, Phys. Rev. Lett. **55**, 1715 (1985).

[14] T. W. Appelquist, M. J. Bowick, D. Karabali, and L. C. R. Wijewardhana, Phys. Rev. **D33**,

3704 (1986).

[15] T. Appelquist, M. J. Bowick, D. Karabali, and L. C. R. Wijewardhana, Phys. Rev. **D33**, 3774 (1986).

[16] T. Appelquist, D. Nash, and L. C. R. Wijewardhana, Phys. Rev. Lett. **60**, 2575 (1988).

[17] A. V. Kotikov, V. I. Shilin, and S. Teber (2016), 1605.01911.

[18] J. Braun, H. Gies, L. Janssen, and D. Roscher, Phys.Rev. **D90**, 036002 (2014), 1404.1362.

[19] T. Appelquist, A. G. Cohen, and M. Schmaltz, Phys. Rev. **D60**, 045003 (1999), hep-th/9901109.

[20] T. Appelquist and L. C. R. Wijewardhana, in *Proceedings, 3rd International Symposium on Quantum theory and symmetries (QTS3)* (2004), pp. 177–191, hep-ph/0403250.

[21] S. Giombi, I. R. Klebanov, and G. Tarnopolsky (2015), 1508.06354.

[22] S. Giombi, G. Tarnopolsky, and I. R. Klebanov (2016), 1602.01076.

[23] L. Di Pietro, Z. Komargodski, I. Shamir, and E. Stamou, Phys. Rev. Lett. **116**, 131601 (2016), 1508.06278.

[24] I. F. Herbut (2016), 1605.09482.

[25] S. M. Chester and S. S. Pufu (2016), 1603.05582.

[26] S. Hands, J. Kogut, and C. Strouthos, Nucl.Phys. **B645**, 321 (2002), hep-lat/0208030.

[27] S. Hands, J. Kogut, L. Scorzato, and C. Strouthos, Phys.Rev. **B70**, 104501 (2004), hep-lat/0404013.

[28] O. Raviv, Y. Shamir, and B. Svetitsky, Phys. Rev. **D90**, 014512 (2014), 1405.6916.

[29] N. Karthik and R. Narayanan, Phys. Rev. **D93**, 045020 (2016), 1512.02993.

[30] S. Hands, Phys. Lett. **B754**, 264 (2016), 1512.05885.

[31] S. Hands, JHEP **09**, 047 (2015), 1507.07717.

[32] R. Narayanan and J. Nishimura, Nucl.Phys. **B508**, 371 (1997), hep-th/9703109.

[33] Y. Kikukawa and H. Neuberger, Nucl.Phys. **B513**, 735 (1998), hep-lat/9707016.

[34] G. Mack, Commun. Math. Phys. **55**, 1 (1977).

[35] J. C. Osborn and J. J. M. Verbaarschot, Nucl. Phys. **B525**, 738 (1998), hep-ph/9803419.

[36] B. Al'tschuler and B. Shklovskii, Sov. Phys. JETP **64**, 127 (1986).

[37] B. Al'tschuler, I. Zharekeshev, S. Kotochigova, and B. Shklovskii, Sov. Phys. JETP **67**, 625 (1988).

[38] V. Chalker, J.T. amd Kravtsov and I. Lerner, Pis'ma v ZhETF **64**, 355 (1996).

[39] R. Narayanan and H. Neuberger, Nucl.Phys. **B443**, 305 (1995), hep-th/9411108.

[40] N. Karthik and R. Narayanan, Phys. Rev. **D92**, 025003 (2015), 1505.01051.

[41] T. Kalkreuter and H. Simma, Comput. Phys. Commun. **93**, 33 (1996), hep-lat/9507023.

[42] J. van den Eshof, A. Frommer, T. Lippert, K. Schilling, and H. A. van der Vorst, Comput. Phys. Commun. **146**, 203 (2002), hep-lat/0202025.

[43] T.-W. Chiu, T.-H. Hsieh, C.-H. Huang, and T.-R. Huang, Phys. Rev. **D66**, 114502 (2002), hep-lat/0206007.

[44] R. G. Edwards, U. M. Heller, and R. Narayanan, Phys.Rev. **D59**, 094510 (1999), hep-lat/9811030.

[45] C. Gattringer and C. Lang, *Quantum chromodynamics on the lattice: An introductory presentation (lecture notes in physics vol. 788)* (2009).

[46] P. Francesco, P. Mathieu, and D. Senechal, *Conformal field theory, graduate texts in contemporary physics* (1999).

[47] J. C. Collins, A. V. Manohar, and M. B. Wise, Phys. Rev. **D73**, 105019 (2006), hep-th/0512187.

[48] L. Janssen (2016), 1604.06354.

[49] N. Karthik and R. Narayanan (in preparation).

[50] B. Sheikholeslami and R. Wohlert, Nucl. Phys. **B259**, 572 (1985).

[51] A. Hasenfratz and F. Knechtli, Phys. Rev. **D64**, 034504 (2001), hep-lat/0103029.

[52] A. Hasenfratz, R. Hoffmann, and S. Schaefer, JHEP **05**, 029 (2007), hep-lat/0702028.

[53] T. A. DeGrand and D. Toussaint, Phys. Rev. **D22**, 2478 (1980).